

Trigonal distortion in the honeycomb iridates: Proximity of zigzag and spiral phases in Na_2IrO_3

Jeffrey G. Rau¹ and Hae-Young Kee^{1,2,*}

¹*Department of Physics, University of Toronto, Toronto, Ontario M5S 1A7, Canada*

²*Canadian Institute for Advanced Research/Quantum Materials Program, Toronto, Ontario MSG 1Z8, Canada*

(Dated: August 22, 2014)

The Kitaev honeycomb model has been suggested as a useful starting point to describe the honeycomb iridates. However, the zigzag ordering seen in Na_2IrO_3 and the magnetic transition in Li_2IrO_3 have raised questions to their connection to the Kitaev model and to the microscopic origin of these magnetic states, given their structural similarities. Here we study how the magnetic phases near the Kitaev spin liquid are affected by the inclusion of trigonal distortion of the oxygen octahedra within a purely nearest neighbour model. Using a combination classical analysis and exact diagonalization we show that near the ferromagnetic Kitaev limit a small amount of trigonal distortion, as found in Na_2IrO_3 , stabilizes a zigzag phase. Decreasing the distortion destabilizes the zigzag phase toward a spiral phase that may be relevant for Li_2IrO_3 . Using semi-classical spin-wave calculations we show that this regime is qualitatively consistent with experimentally known features of the dynamical structure factor in Na_2IrO_3 and speculate on implications for Li_2IrO_3 .

I. INTRODUCTION

The honeycomb iridates Na_2IrO_3 and Li_2IrO_3 have provided a useful playground to study the effects of strong spin-orbit coupling in magnetic materials^{1–11}. Motivation originally stemmed from proposals that these compounds could be proximate to Kitaev’s honeycomb model¹², possibly manifesting its exotic ground state: a gapless \mathbb{Z}_2 spin liquid. Subsequent experiments¹ have proven that this picture incomplete, with both materials exhibiting magnetic order below $\sim 15\text{K}$. In Na_2IrO_3 , resonant inelastic X-ray scattering (RIXS)^{2,9,10} and neutron scattering experiments^{2,4,6} the ordering wave-vector of this magnetic state was determined to be the M point. Further evidence from neutron scattering^{4,6} has shown unambiguously that this ordering forms alternating chains of ferromagnetically aligned spins – the so-called zigzag state.

To explain the appearance of this phase, extensions to the Kitaev model have been proposed. The most studied adds a conventional isotropic Heisenberg coupling in addition to Kitaev terms giving the so-called Heisenberg-Kitaev (HK) model^{13–22}. If indirect oxygen mediated hopping is assumed to be dominant, this model produces a ferromagnetic Kitaev (FK) exchange. However, within the HK model one must lie near the antiferromagnetic Kitaev (AFK) limit to achieve the observed zigzag state (AFK-zigzag) – opposite to the expectation from dominant oxygen mediated hopping. Other proposals consider using significant second and third nearest-neighbour Heisenberg couplings²³ to stabilize a zigzag phase near the FK limit.

While theoretically appealing, the HK model is not the minimal model for the honeycomb iridates, even in the idealized limit, with no trigonal or monoclinic distortions. As shown recently in Ref. 24, at nearest neighbour level an additional term must be included – so-called symmetric off-diagonal exchange Γ , leading to the HK Γ model. Such a term is generically induced when both oxygen mediated and direct overlap of the $5d$ orbitals are present in the underlying microscopic model. This HK Γ model has additional phases appearing near the FK limit, such as incommensurate spirals and further zigzag regions. While these results are suggestive, the trig-

onal compression present in the crystal structure of Na_2IrO_3 should be taken into account.

Recently, the effects of such trigonal distortion of the oxygen octahedra and the monoclinic distortions of the lattice have been considered^{25,26} in ab-initio treatments of Na_2IrO_3 . The results of these calculations suggest a dominant FK coupling, as well as sensitivity of the exchanges to the oxygen positions. While these calculations can stabilize a zigzag ground state (FK-zigzag)^{25,26} and qualitatively reproduce the susceptibility anisotropy²⁶, whether these models can account for the known features of the excitation spectrum seen in RIXS and inelastic neutron scattering (INS) experiments remains to be seen. In this approach, zigzag order is stabilized through the presence of additional anisotropic exchanges as well as further neighbour anisotropic couplings generated due to the inclusion of trigonal and monoclinic distortion. Including these effects complicate the model considerably – at the nearest neighbour level alone ten independent exchange constants must be considered. Due to the large number of phases that meet near the Kitaev limits, it is unclear which of these many interactions is responsible for stabilizing the zigzag order.

In this article we show that when trigonal distortion is included the appearance of the zigzag state can be explained within a purely nearest neighbour model – without the need to appeal to second and third neighbour couplings or significant monoclinic distortion. To make the physics as transparent as possible we work with a model of the Na_2IrO_3 structure that allows us to study the effects of trigonal distortion directly. Through microscopic calculations and symmetry arguments we first generalize the HK Γ model to include the effects trigonal distortion of the oxygen octahedra. We show that this trigonal distortion introduces an additional symmetric off-diagonal exchange Γ' into the spin Hamiltonian. We then analyze this model near the AFK and FK limits using a classical analysis as well as through exact diagonalization. Two distinct zigzag regions are found: near the AFK limit as found in Refs. 20 and 21 and near the FK limit with finite Γ discussed in Ref. 24. The latter zigzag phase is further stabilized by the addition of negative Γ' . To compare with the experimental results we compute the dynamical structure factor using semi-classical spin-wave theory for each zigzag

region. While the the AFK-zigzag can be made qualitatively consistent with the constraints from INS and RIXS experiments, one must tune Γ to be small while keeping K large and positive – without generating an antiferromagnetic J . If oxygen mediated exchange is larger or comparable to the direct dd overlap this regime seems implausible. In the FK regime we find that a zigzag phase with nearly gapless excitations can be stabilized with significant Γ and small negative Γ' . In addition, we find that when Γ' is small or positive values the zigzag phase becomes unstable towards a multiple- Q spiral with dominant wave-vector lying in the first Brillouin zone (BZ). We conclude that with addition of trigonal distortion the the FK-zigzag is qualitatively consistent with the features seen experimentally in Na_2IrO_3 and possibly provides a connection to the ordered phase of Li_2IrO_3 .

The article is organized as follows: in Sec. II we give an overview of the atomic physics of the Ir^{4+} in the presence of trigonal distortion, outlining the derivation of the pseudo-spin model using a strong coupling expansion. Expressions for J , K , Γ and Γ' are presented in a simplified limit, with the full general case and some details presented in Appendix A. In Sec. III we present simulated annealing calculations of the classical phase diagram when Γ' is included, discussing the new multiple- Q incommensurate spiral phases that appear. In Sec. IV we focus on the FK and AFK limits using exact diagonalization of a 24-site cluster, presenting phase diagrams as a function of J and Γ for variety of Γ' . In Sec. V we consider spin-wave calculations of the properties of the FK-zigzag and AFK-zigzag phases found in Sec. III and Sec. IV, discussing the connection to reported experimental results for the dynamical structure factor from INS and RIXS experiments. In Sec. VI we discuss the implications for Na_2IrO_3 as well as the applicability of these results to Li_2IrO_3 .

II. MICROSCOPICS

To derive an effective model that captures the essential physics of Na_2IrO_3 and Li_2IrO_3 we build our description using an idealized version of the crystal structure. We start with an ideal honeycomb lattice surrounded by edge-shared oxygen octahedra, with all monoclinic and trigonal distortions removed. Moving beyond this, we include the effects of trigonal distortions of the oxygen octahedra. We must first identify the relevant degrees of freedom at the Ir site.

A. Local physics

Consider a single IrO_6 octahedron in the absence of interactions; the crystal field provided by the O^{2-} splits the $5d$ orbitals of the Ir^{4+} ion into an e_g doublet and t_{2g} triplet. Since the electronic configuration is $5d^5$ we have a single hole in the t_{2g} and unoccupied e_g levels. Since the energy scale of the octahedral splitting is on the order of a few eV, the e_g levels can be safely neglected. The remaining t_{2g} levels form a pseudo-vector with the angular momentum of the d electrons projected into the t_{2g} subspace is given by $-\vec{L}$ where \vec{L} are

$l = 1$ angular momentum matrices. The single-particle parts of the atomic Hamiltonian have the form

$$-\lambda \vec{L} \cdot \vec{S} + \Delta (\hat{n} \cdot \vec{L})^2, \quad (1)$$

where \hat{n} is a unit vector along the $[111]$ direction. The sign of Δ distinguishes between trigonal compression ($\Delta > 0$) and trigonal expansion ($\Delta < 0$) of the oxygen octahedra. Since $\hat{n} \cdot (\vec{L} + \vec{S})$ is conserved, we rotate the spin and effective orbital angular momentum so that \hat{z} is along \hat{n} . In this basis the Hamiltonian is easily diagonalized (see Ref. 27 for details) giving three doublets

$$|1, \pm\rangle = \cos \theta \left| \frac{1}{2}, \pm \frac{1}{2} \right\rangle_{\hat{n}} \pm \sin \theta \left| \frac{3}{2}, \pm \frac{1}{2} \right\rangle_{\hat{n}} \quad (2a)$$

$$|2, \pm\rangle = \mp \sin \theta \left| \frac{1}{2}, \pm \frac{1}{2} \right\rangle_{\hat{n}} + \cos \theta \left| \frac{3}{2}, \pm \frac{1}{2} \right\rangle_{\hat{n}} \quad (2b)$$

$$|3, \pm\rangle = \left| \frac{3}{2}, \pm \frac{3}{2} \right\rangle_{\hat{n}} \quad (2c)$$

where $|j, m\rangle_{\hat{n}}$ are the effective $j = 1/2$ and $j = 3/2$ states quantized with \hat{z} along the $[111]$ direction. The angle θ parametrizes the relative strength of trigonal distortion and spin-orbit coupling

$$\tan(2\theta) = \frac{4\sqrt{2}\Delta}{2\Delta + 9\lambda}. \quad (3)$$

Note that for small trigonal distortion $\theta \sim 2\sqrt{2}\Delta/9\lambda$. The energies of these states are given by

$$E_1 = \frac{1}{2} \left(\frac{\lambda}{2} + \Delta \right) + \sqrt{\frac{1}{4} \left(\frac{\Delta}{3} + \frac{3\lambda}{2} \right)^2 + \frac{2\Delta^2}{9}}, \quad (4a)$$

$$E_2 = \frac{1}{2} \left(\frac{\lambda}{2} + \Delta \right) - \sqrt{\frac{1}{4} \left(\frac{\Delta}{3} + \frac{3\lambda}{2} \right)^2 + \frac{2\Delta^2}{9}}, \quad (4b)$$

$$E_3 = \Delta - \frac{\lambda}{2}. \quad (4c)$$

In the absence of spin-orbit coupling (near $\theta = \tan^{-1}(2\sqrt{2})/2$) this term splits the t_{2g} levels in an a_{1g} singlet and e_g doublet, with the energy difference given by Δ . When both trigonal distortion and spin-orbit coupling are included the t_{2g} levels split into three Kramers doublets with the degeneracy fully lifted. In this case the relevant degrees of freedom are in the highest-lying doublet which is half-filled. When trigonal distortion is zero (near $\theta = 0$), the three t_{2g} orbitals form an effective $l = 1$ pseudo-vector, with spin-orbit coupling splitting these into a $j = 1/2$ doublet and $j = 3/2$ quartet. The five d electrons fill the $j = 3/2$ states completely, leaving a single electron in the $j = 1/2$ doublet. This $j = 1/2$ doublet adiabatically connects to the $|1, \pm\rangle \equiv |\pm\rangle$ doublet for all values of Δ/λ and thus represents our low energy degrees of freedom.

We note that the full distortion (both monoclinic and trigonal) of the oxygen octahedra in Na_2IrO_3 lowers the symmetry at the Ir site to $2/m$: a single C_2 rotation and reflection. In Na_2IrO_3 , the trigonal distortion is seen clearly if one looks at the difference between in the oxygen-oxygen distances for

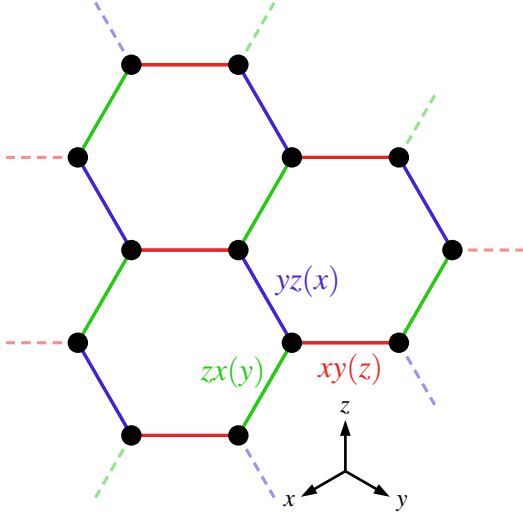


FIG. 1: Notation for the Kitaev and bond-dependent exchanges. We have denoted the $yz(x)$ bonds blue, the $zx(y)$ bonds green and the $xy(z)$ bonds red. The choice of x, y and z axes is also shown.

bonds that lie in the $[111]$ plane and those that do not⁶. While the in-plane bonds are separated by $\sim 3.01 - 3.03\text{\AA}$, the other bonds vary from $2.65 - 2.97\text{\AA}$. In Li_2IrO_3 the site symmetry is reduced to a single two-fold rotation, a single C_2 rotation²⁸. The difference between the bonds in the $[111]$ plane and the others is also less pronounced, although there is still large variations between the different bonds due to monoclinic distortion. This is consistent with estimates of the change of the trigonal distortion in these compounds from magnetic susceptibility measurements¹¹. Generically, inclusion all of these distortions gives three Kramers doublets, as in the case with just trigonal distortion. For simplicity we will ignore such further small corrections to the $|\pm\rangle$ doublet from these monoclinic distortions, as our goal is to isolate and study the effects of trigonal distortion.

B. Tight-binding model

With the local degrees of freedom identified, we now consider hopping processes between Ir atoms. This contribution to the Hamiltonian has the form

$$H_{\text{kinetic}} = \sum_{\langle ij \rangle} \sum_{\alpha\beta} d_{i\alpha}^\dagger t_{ij}^{\alpha\beta} d_{j\beta}, \quad (5)$$

where $d_{i\alpha}^\dagger = (d_{i\alpha\uparrow}^\dagger, d_{i\alpha\downarrow}^\dagger)$ and $d_{i\alpha}$ are the creation and annihilation operators for the t_{2g} state α at site i . To clarify what is possible, we first look at how the symmetry of the model constrains the hopping terms. Consider a nearest neighbour Ir-Ir bond of type $xy(z)$ as shown in Fig. 1. The relevant processes that contribute to these hoppings will involve mainly the two Ir^{4+} ions and their respective O^{2-} octahedral cages. The symmetries of this complex then constraint the hopping matrix. When the octahedra are ideal, these symmetries in-

clude inversion through the bond center, time-reversal as well as C_2 rotations along the $[1\bar{1}0]$ and $[001]$ axes. For example, time-reversal and inversion force the matrix to be both real and symmetric, while the presence of the C_2 axis along $[1\bar{1}0]$ requires $t_{yz,xy}^z = t_{zx,xy}^z$ and $t_{zx,zx}^z = t_{yz,yz}^z$. If the all symmetries are used, the hopping matrix on this bond is then constrained to the form

$$t_{xy(z)} = \begin{pmatrix} t_1 & t_2 & 0 \\ t_2 & t_1 & 0 \\ 0 & 0 & t_3 \end{pmatrix}, \quad (6)$$

where the basis is ordered yz, zx and xy . The presence of the C_2 about $[001]$ is what prevents any mixing between the xy orbital and the zx and yz orbital, forcing $t_{yz,xy}^z = t_{zx,xy}^z = 0$. If we consider the symmetries of the true space group $C2/m$ which are present, then this C_2 about $[001]$ is lost. This results in an additional allowed term, giving the more general form

$$t_{xy(z)} = \begin{pmatrix} t_1 & t_2 & t_4 \\ t_2 & t_1 & t_4 \\ t_4 & t_4 & t_3 \end{pmatrix}. \quad (7)$$

When monoclinic distortion is neglected, the kinetic terms for the $yz(x)$ and $zx(y)$ bonds can be found using the rotational symmetry of the lattice from those of the $xy(z)$ bond. Rotating the t_{2g} orbitals we then arrive at the hopping matrices

$$t_{yz(x)} = \begin{pmatrix} t_3 & t_4 & t_4 \\ t_4 & t_1 & t_2 \\ t_4 & t_2 & t_1 \end{pmatrix}, \quad t_{zx(y)} = \begin{pmatrix} t_1 & t_4 & t_2 \\ t_4 & t_3 & t_4 \\ t_2 & t_4 & t_1 \end{pmatrix}. \quad (8)$$

When the distortions are included the $yz(x)$ and $zx(y)$ must be analyzed separately, with hopping parameters distinct from the $xy(z)$ bond. Further, the $yz(x)$ and $zx(y)$ bonds do not possess the C_2 axis and thus are only required to be real and symmetric. However, in this case the $yz(x)$ and $zx(y)$ are not independent as the C_2 axis about the $xy(z)$ bond relates the hopping matrices. Putting these all together, the kinetic Hamiltonian can be then written in the compact form

$$\sum_{\langle ij \rangle \in \alpha\beta(\gamma)} \left[t_1 (d_{i\alpha}^\dagger d_{j\alpha} + d_{i\beta}^\dagger d_{j\beta}) + t_2 (d_{i\alpha}^\dagger d_{j\beta} + d_{i\beta}^\dagger d_{j\alpha}) + t_3 d_{i\gamma}^\dagger d_{j\gamma} + t_4 (d_{i\gamma}^\dagger d_{j\alpha} + d_{i\gamma}^\dagger d_{j\beta} + d_{i\alpha}^\dagger d_{j\gamma} + d_{i\beta}^\dagger d_{j\gamma}) \right], \quad (9)$$

where we sum over the $yz(x)$, $zx(y)$ and $xy(z)$ links as indicated in Fig. 1, mapping the directions to orbitals as $x \rightarrow yz$, $y \rightarrow zx$ and $z \rightarrow xy$.

There are several processes that generate such kinetic terms for the Ir t_{2g} orbitals. Two important mechanisms are direct dd overlap and oxygen mediated hopping. Considering again the $xy(z)$ bond, each type of hopping can be written using a Slater-Koster scheme²⁹, expressing the amplitudes in terms of the dd and pd parameters. We begin with the fully idealized structure. Given the large $t_{pd\pi}$ overlap, we have taken the oxygen-mediated parts to be dominant. This contributes an zx - yz inter-orbital hopping of order $t_{pd\pi}^2/\Delta_{pd}$ where Δ_{pd} is the Ir-O charge gap. When projected into the $j = 1/2$ subspace this inter-orbital term vanishes, so we must consider further contributions. The simplest to include is direct overlap of the

5d orbitals which induces both intra- and inter-orbital terms. Putting these contributions together we have

$$t_1 = t^{yz,yz} = \frac{t_{dd\pi} + t_{dd\delta}}{2}, \quad (10a)$$

$$t_2 = t^{yz,zx} = \frac{t_{pd\pi}^2}{\Delta_{pd}} + \frac{t_{dd\pi} - t_{dd\delta}}{2}, \quad (10b)$$

$$t_3 = t^{xy,xy} = \frac{3t_{dd\sigma} + t_{dd\delta}}{4}. \quad (10c)$$

Further contributions are possible to each of t_1 , t_2 and t_3 . For example, hopping mediated through the central Na introduces a contribution to t_2 of order $t_{sd\sigma}^2/\Delta_{sd}$ where $t_{sd\sigma}$ is the overlap between the Na 3s and the Ir 5d orbitals and Δ_{sd} being the Na-Ir charge gap. The addition of trigonal compression of the oxygen octahedra allows for t_4 to become non-zero. This occurs since the oxygens tilt out of the xy plane of the bond, breaking the C_2 symmetry about [001]. The inclusion of trigonal distortion thus induces two distinct effects: the change in the local atomic states and through the generation of these additional kinetic terms.

C. Strong-coupling limit

The relevant degree of freedom in the strong-coupling limit is a pseudo-spin \vec{S}_i at each site originating from the half-filled doublet. In the most idealized case, this doublet effectively has $j = 1/2$ and so the spin operators transform like a pseudo-vector. This remains true even as trigonal distortion is introduced. Considering the symmetry of the $xy(z)$ bond discussed in the previous section, the allowed exchanges are constrained in manner identical to that of the t_{2g} hoppings, as they transform in the same way under symmetry. We thus see that without trigonal distortion the allowed exchanges for a $xy(z)$ from site i to j are of three types: Heisenberg exchange J , Kitaev exchange K and symmetric off-diagonal exchange Γ . Making this relationship explicit, the exchange t_1 is analogous to J , the exchange t_3 to $J + K$ and the t_2 to the exchange Γ . Extending this to $yz(x)$ and $zx(y)$ bonds we have the spin Hamiltonian

$$\sum_{\langle ij \rangle \in \alpha\beta(\gamma)} \left[J \vec{S}_i \cdot \vec{S}_j + K S_i^\gamma S_j^\gamma + \Gamma (S_i^\alpha S_j^\beta + S_i^\beta S_j^\alpha) \right]. \quad (11)$$

When trigonal distortion is included then we have an additional term; we will call this contribution Γ' and it takes the form

$$\Gamma' \sum_{\langle ij \rangle \in \alpha\beta(\gamma)} \left[S_i^\alpha S_j^\gamma + S_i^\gamma S_j^\alpha + S_i^\beta S_j^\gamma + S_i^\gamma S_j^\beta \right]. \quad (12)$$

In the language of symmetry this is analogous to the t_4 contribution to the hopping Hamiltonian. In the absence of monoclinic distortion this is most general nearest-neighbour spin model allowed for these doublets.³⁰

To see how these exchanges arise from the underlying microscopic theory we carry about a strong-coupling expansion. There are several limits depending on the order in which the energy scales are taken to be large. Two limits under which this is tractable analytically are $U, J_H \gg \lambda, \Delta \gg t$ and

$U, \lambda \gg J_H \gg \Delta \gg t$. We will consider the former case as it is most commonly used in the literature and illustrates how each contribution appears in the exchanges. We stress that the results do not depend strongly on which limit is used. To begin, we assume an atomic Hamiltonian of Kanamori form³¹:

$$H_0 = \sum_i \left[\frac{U - 3J_H}{2} (N_i - 5)^2 - 2J_H S_i^2 - \frac{J_H}{2} L_i^2 \right], \quad (13)$$

where N_i , S_i , and L_i are the total number, spin, and (effective) orbital angular momentum operators at site i , U is the Coulomb interaction, and J_H is Hund's coupling. Since the spin-orbit coupling and trigonal distortion then dominate the kinetic terms, the resulting spin-orbital model can be projected into the subspace of the $|1, \pm\rangle$ doublet³² shown in Eq. 2a. As in Section II A we will work with the quantization axis along the [111] direction, so the states shown in Eq. 2a can be used directly. Note that this requires the hoppings to be rotated into this basis as well. Treating the kinetic terms as a perturbation yields the Hamiltonian given in Eqs. 11-12. Due to the complexity of expressions we leave a full presentation of these expressions for Appendix A and consider some simple limiting regimes. We will treat the trigonal distortion as small, expanding the expressions to order θ . We first consider the case where the oxygen mediated and $dd\sigma$ overlap are the dominant kinetic processes with $t_1, t_4 \sim 0$ and $t_2, t_3 \neq 0$.

$$\begin{aligned} J &= \frac{4}{27} \left[\frac{2t_3^2 + 4\sqrt{2}\theta t_2 t_3}{U - J_H} - \frac{12\sqrt{2}\theta t_2 t_3}{U - 3J_H} + \frac{t_3^2 + 4\sqrt{2}\theta t_2 t_3}{U + 2J_H} \right], \\ K &= -\frac{8J_H}{9} \left[\frac{3t_2^2 - t_3^2 - 2\sqrt{2}\theta t_2 t_3}{(U - 3J_H)(U - J_H)} \right], \\ \Gamma &= -\frac{8J_H}{9} \left[\frac{2t_2 t_3 + \sqrt{2}\theta(t_2^2 + t_3^2)}{(U - 3J_H)(U - J_H)} \right], \\ \Gamma' &= -\frac{8J_H}{9} \left[\frac{\sqrt{2}\theta((t_2 + t_3)^2 + 4t_2^2)}{2(U - 3J_H)(U - J_H)} \right]. \end{aligned} \quad (14)$$

The leading terms of these expressions have the same form as seen in Ref. 24, with additional contributions of order θ . Considering the microscopic origins, we expect $t_2 \sim t_{d\pi}^2/\Delta_{pd} > 0$ and $t_3 \sim t_{dd\sigma} < 0$ with $t_2 > |t_3|$. This leads to $K < 0$, $\Gamma > 0$ with J and Γ' being subleading in t_2 . The contribution to Γ' is directly proportional to θ with $\Gamma' < 0$ appearing for trigonal compression and $\Gamma' > 0$ appearing for trigonal expansion. As J is subleading, its sign will depend on the detailed strengths of t_1 , t_3 and the other contributions that are given in Appendix A. As most of our subsequent results are insensitive to the sign of J , we will not try to pin down its value more precisely. We note that additional contributions to Γ' could change the sign of Γ' , see for example the full expressions in Appendix A.

III. CLASSICAL PHASE DIAGRAM

To gain some understanding of this model we first map out the classical phase diagram for arbitrary J , K and Γ with small

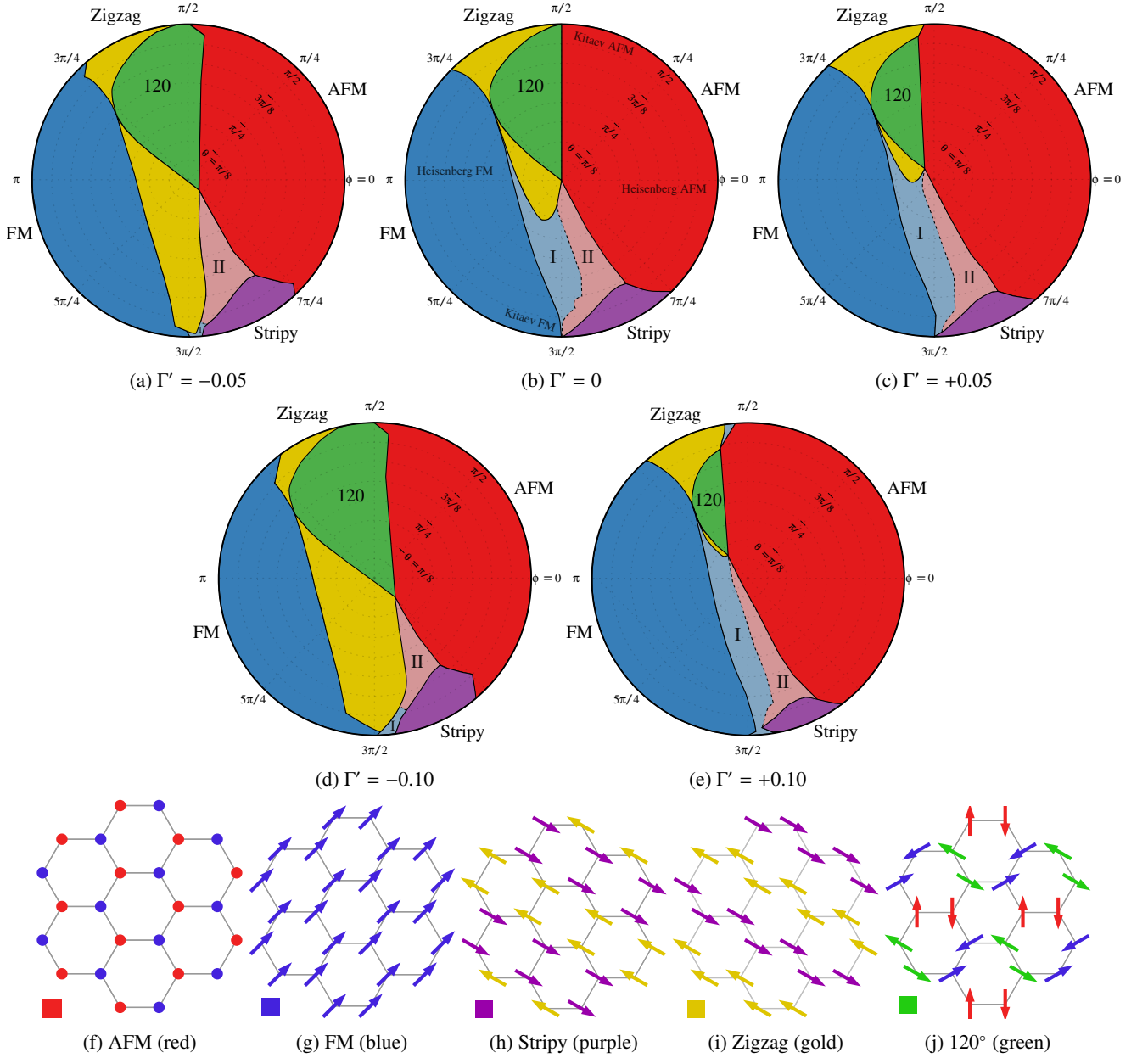


FIG. 2: (a-e) Classical phase diagrams obtained through simulated annealing (see main text for details) for a variety of values of Γ' . (f-g) Representative ground state spin configurations in each classical commensurate phase, with the corresponding colour in the phase diagrams of (a-e) given in brackets.

Γ' . To do this we use simulated annealing on finite clusters with $2 \cdot 12^2$ and $2 \cdot 24^2$ sites to relax to the classical ground state using a single-spin Metropolis updating procedure. For each point in parameter space we perform $2 \cdot 10^6$ sweeps with 10 different starting points, taking the state with lowest energy as the classical ground state. The results of the two clusters are in qualitative agreement throughout the phase diagram.

The full phase diagrams for several values of Γ' are shown in Fig. 2. We have normalized the energy scale so that $J^2 + K^2 + \Gamma^2 = 1$ and parametrized

$$J = \sin \theta \cos \phi, \quad K = \sin \theta \sin \phi, \quad \Gamma = \cos \theta, \quad (15)$$

allowing Γ' to vary freely. As in the single- Q analysis of Ref. 24 we find five commensurate phases: the ferromagnet (FM), antiferromagnet (AFM), stripy, zigzag and 120° are shown in Figs. 2f-2j. Beyond these single- Q phases, there are two families of multiple- Q incommensurate spiral phases that appear at finite Γ and Γ' , we have labeled these phases I and II. We have roughly classified these phases through the wave-vector of the largest components of the static structure factor: if it lies in the first Brillouin zone then it is in phase I, while if it lies outside then it is labeled II. Each of these phases has additional peaks and the position of dominant wave-vector seems

to vary continuously throughout each phase. By this we mean that as the cluster size is increased the number of distinct dominant wave-vectors in each phase increases; the regions of a given wave-vector become smaller and the behaviour becomes more like a smooth gradient. We note that for small Γ' there is a large region in phase I with dominant wave-vector $2M/3$ in our finite size calculations. Within the clusters used it is unclear whether this parameter regime is truly commensurate or incommensurate in the thermodynamic limit, as the wave-vector could be simply changing too slowly for our finite size calculations to resolve. In the case with larger negative $\Gamma' = -0.10$ this dominant wave-vector appears to tune continuously through from $\vec{Q} = 0$ (FM) to the maximal \vec{Q} wave-vector (AFM). While the zigzag phase does not appear adjacent to the FK limit for $\Gamma' = 0$, the nearby phase I is highly sensitive to the presence of Γ' . For even a small negative Γ' we see in Fig. 2a that phase I becomes unstable to the zigzag order. This persists for larger negative Γ' , with a zigzag phase close to the FK limit, as seen in Fig 2d. With positive Γ' the opposite occurs; the zigzag phase is suppressed giving way to larger I, II, FM and AFM phases, as seen in Figs 2c and 2e. We note that the wave-vector of phases I and II are dependent on the value of Γ' . Given the weakness of phases I and II, as well as the enhancement of the zigzag phase by quantum fluctuations²⁴ the relevance of these phases to the full quantum mechanical model at $\Gamma' = 0$ remains unclear. We note that at least classically both the AFK-zigzag and FK-zigzag phase border incommensurate spiral phases.

IV. QUANTUM PHASE DIAGRAM

We now compare this classical analysis to exact diagonalization study of a 24-site cluster. This cluster has been used in previous studies of the HK^{13,20,21} and HKI²⁴ model as it is compatible with most the classical orders of the model as well as the four-sublattice duality transformation that relates the FM and AFM phases to the stripy and zigzag. The phases were identified by examining the spin-spin correlation functions $\langle S_i^\alpha S_j^\beta \rangle$, primarily through the static structure factor

$$S(\vec{Q}) = \frac{1}{N} \sum_{ij} e^{i\vec{Q} \cdot (\vec{r}_i - \vec{r}_j)} \langle \vec{S}_i \cdot \vec{S}_j \rangle, \quad (16)$$

in both the original basis and after applying the four-sublattice rotation. We note that this four-sublattice rotation is not a duality transformation when Γ or Γ' is included, but still provides a useful indicator given the structure of the well-understood stripy and zigzag phases in the HK limit. Motivated by the large diversity of phases that meet at the AFK and FK limits in the classical calculations, as well as the ab-initio results of Refs. 25 and 26 we will focus on the FK and AFK limits in our exact diagonalization. To this end we fix the energy scale so that $K = \pm 1$, leaving three parameters J , Γ and Γ' . We show these phase diagrams for slices of constant Γ' near $\Gamma' = 0$, with J and Γ varying, as seen in Fig. 3.

Due to the qualitative similarity between the classical and quantum results, we can directly identify the FK-zigzag and

AFK-zigzag in these results. The zigzag phase near the AFK limit is connected to the zigzag phase seen in the HK model as studied in Refs. 20 and 21. Appearing only when $J < 0$, this phase is stable to finite Γ , but is eventually suppressed at large enough Γ' . The FK-zigzag only appears when Γ is finite as noted in Refs. 24 and 25 but is quite weak in these exact diagonalization calculations. We see here that the addition of negative Γ' stabilizes this phase; significantly enlarging the zigzag region. To gain further insight into these phases, we look to the structure of excitations above the zigzag ground states.

V. SPIN WAVES

The most detailed information on the magnetic state found in Na_2IrO_3 are based on RIXS and INS data^{6,9}. The high energy spin-wave branch seen in RIXS⁹ with an energy scale of $\sim 30 - 40\text{meV}$ points towards exchanges on the order of hundreds of K . This makes direct extraction of information from the susceptibility difficult as current experiments do not probe the high-temperature regime. Further, the energies seen in RIXS are quite broad, leaving uncertainty in the dispersion of this mode. The INS data⁶ is more informative, showing two well-defined features: magnetic excitations down to 2meV and a drop off in scattering at low energy with a concave edge in $\omega - |\vec{Q}|$ space. The presence of these low energy excitations bounds the spin-wave gap, constraining any anisotropic terms in the spin Hamiltonian. While quite limited due the lack of directional dependence, the INS remains the only experimental input into the low energy magnetic excitations of Na_2IrO_3 .

To connect our model with these scattering experiments we will use leading order semi-classical spin-wave theory. Within this approximation we compute the inelastic structure factor in the zigzag phases found in the previous sections. Given the strong similarity between the classical and exact diagonalization phase diagrams we expect the spin-wave results to be qualitatively correct. At leading order in $1/S$ we express the spin operators using the Holstein-Primakoff representation

$$\vec{S}_r \sim (S - a_r^\dagger a_r) \hat{z}_r + \sqrt{\frac{S}{2}} [(\hat{x}_r - i\hat{y}_r) a_r^\dagger + (\hat{x}_r + i\hat{y}_r) a_r], \quad (17)$$

where a_r and a_r^\dagger are the Holstein-Primakoff bosons and $(\hat{x}_r \hat{y}_r \hat{z}_r)$ define a local frame at site r with \hat{z}_r being the local magnetic ordering direction. The dynamic spin structure factor (at zero temperature) is proportional to

$$S^{\mu\nu}(\vec{Q}, \omega) \propto \sum_{n \neq 0} \delta(\omega - E_n) \langle 0 | S_Q^\mu | n \rangle \langle n | S_{-Q}^\nu | 0 \rangle, \quad (18)$$

where S_Q^μ is the Fourier transform of the spin operator S_r^μ and $\mu = x, y, z$. We will be interested in the inelastic neutron scattering cross section which can be expressed in terms of the structure factor via

$$I(\vec{Q}, \omega) = \frac{d^2\sigma}{d\Omega d\omega} \propto \sum_{\mu\nu} \left(1 - \frac{Q_\mu Q_\nu}{Q^2}\right) S^{\mu\nu}(\vec{Q}, \omega). \quad (19)$$

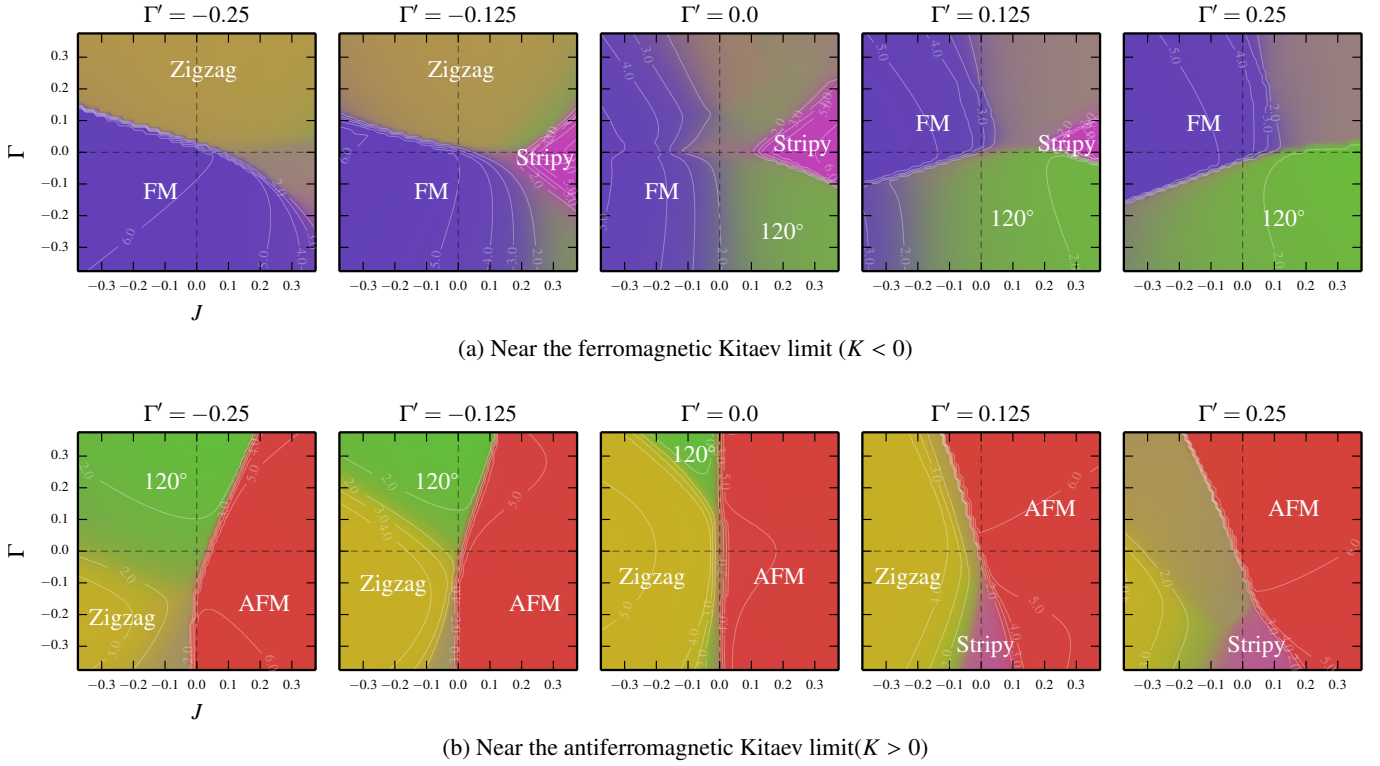


FIG. 3: Phase diagrams from exact-diagonalization of the 24-site cluster. Results are shown near the (a) ferromagnetic ($K < 0$) and (b) antiferromagnetic ($K > 0$) Kitaev limits as a function of J , Γ and Γ' with the energy scale fixed so $|K| = 1$. Colours identify the phases: FM (blue), AFM (red), zigzag (gold), stripy (magenta), 120° (green). The colour corresponds to values of the static structure factor S_Q in the original or rotated basis. Contours of constant S_Q are shown for the dominant wave-vector in each region.

For simplicity we have not included anisotropic g factors in these expressions. We present these results showing a plot of the spin wave spectrum around the path $X-\Gamma-Y-\Gamma'-M-\Gamma$ ²⁰. The colours indicate the magnitude of $I(\vec{Q}, \omega)$ after convolving the structure factor with a gaussian of finite width to emulate finite experimental resolution.

VI. DISCUSSION

First, let us discuss the dependence of the M point spin-wave gap on the parameters J, K, Γ and Γ' in each of the zigzag phases. In the AFK limit, earlier studies²⁰ have pointed out the accidental $SO(3)$ degeneracy of the classical ground state manifold in the HK limit. This pseudo-symmetry manifests in the semi-classical calculations through the appearance of gapless excitations near the M point – even though spin rotation symmetry is strongly broken by spin-orbit effects. The addition of Γ and Γ' affect these pseudo-Goldstone modes differently. Moving away from the HK limit via Γ immediately gaps out the M point, with the gap equal to $\sim |\Gamma|$. We see then we can bound $|\Gamma|$ to be smaller than $\sim 1 - 2\text{meV}$ due to the low energy cutoff to the INS data. Curiously, adding Γ' to the AFK-zigzag state does not gap out pseudo-Goldstone modes; the $SO(3)$ degeneracy remains unbroken. Ignoring then the

microscopic route to the AFK-zigzag regime, the INS data can be made qualitatively consistent with this phase so long as Γ is small, irrespective of the value of Γ' . Further, to get spin-waves that match the scales seen in the RIXS experiments one needs a large value for K . For a representative point in the AFK-zigzag phase, we choose $J = -10\text{meV}$, $K = 40\text{meV}$, $\Gamma = 1\text{meV}$ and $\Gamma' = 5\text{meV}$. The spin-wave spectrum for these parameter values is qualitatively similar to that reported for the AFK-zigzag in the HK-model²⁰, except for a small gap opened by finite Γ and the splitting of some accidental degeneracies in the spin-wave bands.

The case of the FK limit is more interesting. We first note that within the classical and semi-classical calculations a meta-stable zigzag phase appears over a wide region of parameter space that connects directly to the FK point. This meta-stable state is close in energy to phase I and accounts for its fragility under the addition of a small negative Γ' . Given the enhancement of the zigzag order seen in the exact diagonalization calculations we will discuss this zigzag phase on equal footing with the stable zigzag phase seen when Γ' is finite and sufficiently negative. Start from the FK limit with $J = \Gamma = \Gamma' = 0$. As we increase Γ the zigzag phase immediately opens a gap, with a narrow band of low energy excitations; a remnant of the flat band present at the FK point. As Γ is increased further the gap reaches a maximum then begin

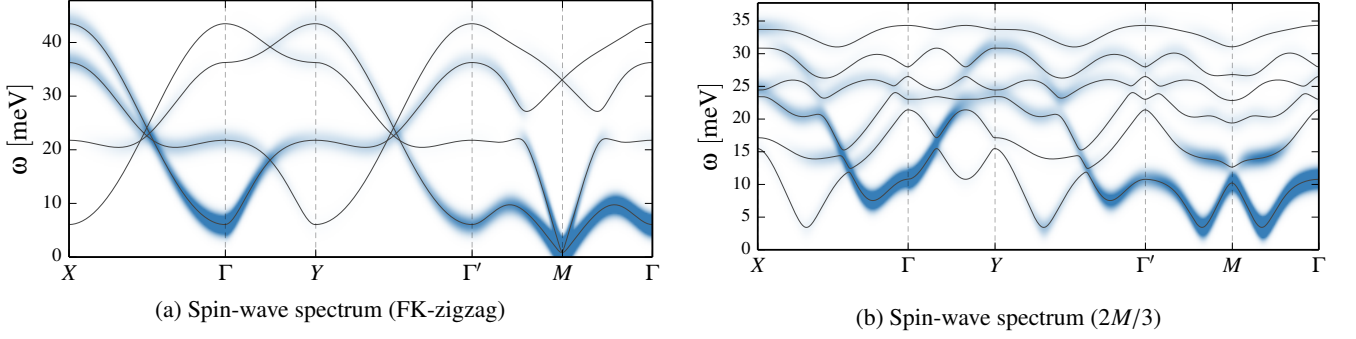


FIG. 4: Spin waves for (a) the FK-zigzag with $J = -8\text{meV}$, $K = -25\text{meV}$, $\Gamma = 20\text{meV}$ and $\Gamma' = -2\text{meV}$. and for (b) the $2M/3$ state of phase I with $J = -3\text{meV}$, $K = -25\text{meV}$, $\Gamma = 20\text{meV}$ and $\Gamma' = 0\text{meV}$. Spin-wave spectrum with the inelastic cross-section $I(\vec{Q}, \omega)$ shown convolved with a gaussian to aid visualization.

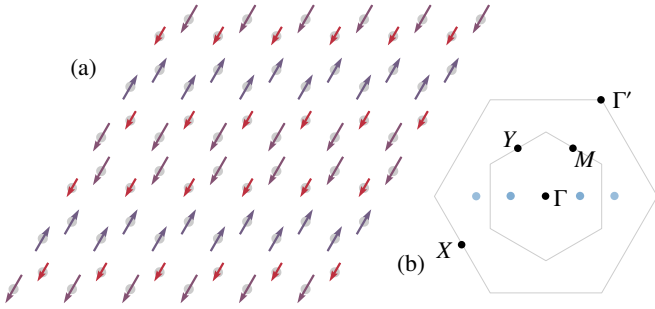


FIG. 5: (a) Spin configuration in the ferrimagnetic $2M/3$ phase, with the spins projected into the honeycomb plane. Deviation out of the honeycomb plane is indicated by colour, with red being into and blue being out of the plane. (b) Static structure factor for this spin configuration, with intensity of colour denoting size of $\vec{S}_Q \cdot \vec{S}_{-Q}$.

decreasing again – finally becoming gapless at the M point at $\Gamma = 4|K|/5$. This is independent of J , one finds a line of gapless points in the meta-stable zigzag phase. At finite Γ' one can still tune to this regime (independent of J), but the zigzag phase is still not the true ground state. To render such a zigzag state stable at the classical level one must add a negative Γ' . This has the effect of opening a gap $\sim |\Gamma'|/2$ in the spin-waves at the M point (the proportionality constant varies weakly as a function of J). Due to the closeness in energy of phase I and the zigzag, the required Γ' is small and can be consistent with the INS bound so long as $|\Gamma'|$ is less than $\sim 1 - 2\text{meV}$. We have shown an example of the spin-wave spectrum of such an FK-zigzag phase in Fig. 4a. The weight of each spin-wave branch is indicated as it appears in the dynamical structure factor by the intensity of the color (convolved with a gaussian to aid visualization). Experimentally⁶, one observes a region with little scattering at low momenta, bounded by a curve that appears to terminate near $|\vec{Q}| = |M|$. The low-energy, high-weight branch that runs from M to Γ in Fig. 4a qualitatively reproduces such behaviour. We note that this zigzag phase persists for positive J , keeping these low-energy features, but differing in some high-energy details.

If we are in the FK-zigzag regime in Na_2IrO_3 then we may be nearby in parameter space for Li_2IrO_3 , with a smaller negative or positive value for Γ' . In the classical analysis this puts us in the regime of phase I. At for the finite-size clusters used in these calculations the ground state in this regime is given by a multiple- Q state with a dominant wave vector at $2M/3$, as mentioned in Sec. III. This state has a tripled unit-cell and carries a finite ferrimagnetic moment of ~ 0.254 per site. The spin configuration projected into the honeycomb plane is shown in Fig. 5. The spin-wave spectrum in this phase for $J = -3\text{meV}$, $K = -25\text{meV}$, $\Gamma = 20\text{meV}$ and $\Gamma' = 0\text{meV}$ is shown in Figs. 4b. Besides a sizable spin-wave gap of order $\sim 4\text{meV}$, we would like to draw attention to the minima in the spin-wave spectrum near multiples of $M/3$, in particular near $2M/3$. This is due to proximity to a classical degeneracy when $J = \Gamma' = 0$ and there are gapless spin-waves. This appears as a low-energy dip in the integrated spectrum near $\sim 0.4\text{\AA}^{-1}$. We note that the magnitude of this wave-vector the inelastic features are in rough agreement with recent reports of inelastic neutron scattering³³. We note that these results hinge on the reliability of the classical ground states. Given the small energy scales involved, quantum mechanical effects may change some of the details of the state. Given the difference in trigonal distortion from Na_2IrO_3 , a state related to this $2M/3$ phase may be relevant for Li_2IrO_3 .

VII. CONCLUSIONS

In summary, we have analyzed a minimal nearest neighbour spin model for the honeycomb iridates including the effects of trigonal distortion derived from microscopic and symmetry arguments. Using classical simulated annealing calculations and exact diagonalization of the full quantum mechanical model, we mapped out the effects of this perturbation on the phase diagram. We identified two distinct zigzag phases: the AFK-zigzag and the FK-zigzag which is stabilized by trigonal distortion. Based on the difficulty of finding an AFK coupling while simultaneously tuning Γ to be small, we argued that the FK-zigzag with significant Γ and small negative Γ' is the likely candidate for Na_2IrO_3 . Looking at the dynam-

ical structure factor within semi-classical spin-wave theory, we showed that this FK-zigzag phase can be made qualitatively consistent with the experimental INS and RIXS data. We further showed that decreasing the trigonal distortion in this parameter regime we find a family of multiple- Q incommensurate spiral phases. Given the smaller trigonal distortion in Li_2IrO_3 , we discussed whether this phase I could be relevant for the magnetically ordered phase in this material. Using a nearby commensurate phase with dominant wave-vector $2M/3$, we showed that this spiral phase is expected to have a gap with the lowest energy scattering occurring near wave-vector $2M/3$.

Note added: After completion of this work, two preprints appeared; Ref. 34 discussing the nature of the ordered phase of Li_2IrO_3 and Ref. 35 discussing the origins of the zigzag phase in Na_2IrO_3 .

ACKNOWLEDGMENTS

We would like to thank Eric Kin-Ho Lee and Yong-Baek Kim for useful discussions. Computations were performed on the GPC supercomputer at the SciNet HPC Consortium. SciNet is funded by: the Canada Foundation for Innovation under the auspices of Compute Canada, the Government of Ontario, Ontario Research Fund - Research Excellence; and the University of Toronto. This work was supported by the NSERC of Canada and the Centre for Quantum Materials at the University of Toronto. HYK acknowledges the hospitality of Aspen Center for Physics (NSF Grant No. PHYS-1066293), where this work was finalized.

-
- * Electronic Address: hykee@physics.utoronto.ca
- ¹ Y. Singh and P. Gegenwart, *Phys. Rev. B* **82**, 064412 (2010).
 - ² X. Liu, T. Berlijn, W.-G. Yin, W. Ku, A. Tsvelik, Y.-J. Kim, H. Gretarsson, Y. Singh, P. Gegenwart, and J. Hill, *Phys. Rev. B* **83**, 220403 (2011).
 - ³ Y. Singh, S. Manni, J. Reuther, T. Berlijn, R. Thomale, W. Ku, S. Trebst, and P. Gegenwart, *Phys. Rev. Lett.* **108**, 127203 (2012).
 - ⁴ F. Ye, S. Chi, H. Cao, B. C. Chakoumakos, J. A. Fernandez-Baca, R. Custelcean, T. Qi, O. Korneta, and G. Cao, *Phys. Rev. B* **85**, 180403 (2012).
 - ⁵ S. Lovesey and A. Dobrynin, *J. Phys. Condens. Matter* **24**, 382201 (2012).
 - ⁶ S. K. Choi, R. Coldea, A. N. Kolmogorov, T. Lancaster, I. I. Mazin, S. J. Blundell, P. G. Radaelli, Y. Singh, P. Gegenwart, K. R. Choi, S.-W. Cheong, P. J. Baker, C. Stock, and J. Taylor, *Phys. Rev. Lett.* **108**, 127204 (2012).
 - ⁷ R. Comin, G. Levy, B. Ludbrook, Z.-H. Zhu, C. N. Veenstra, J. A. Rosen, Y. Singh, P. Gegenwart, D. Stricker, J. N. Hancock, D. van der Marel, I. S. Elfimov, and A. Damascelli, *Phys. Rev. Lett.* **109**, 266406 (2012).
 - ⁸ J. P. Clancy, N. Chen, C. Y. Kim, W. F. Chen, K. W. Plumb, B. C. Jeon, T. W. Noh, and Y.-J. Kim, *Phys. Rev. B* **86**, 195131 (2012).
 - ⁹ H. Gretarsson, J. P. Clancy, Y. Singh, P. Gegenwart, J. P. Hill, J. Kim, M. H. Upton, A. H. Said, D. Casa, T. Gog, and Y.-J. Kim, *Phys. Rev. B* **87**, 220407 (2013).
 - ¹⁰ H. Gretarsson, J. P. Clancy, X. Liu, J. P. Hill, E. Bozin, Y. Singh, S. Manni, P. Gegenwart, J. Kim, A. H. Said, D. Casa, T. Gog, M. H. Upton, H.-S. Kim, J. Yu, V. M. Katukuri, L. Hozoi, J. van den Brink, and Y.-J. Kim, *Phys. Rev. Lett.* **110**, 076402 (2013).
 - ¹¹ G. Cao, T. Qi, L. Li, J. Terzic, V. Cao, S. Yuan, M. Tovar, G. Murthy, and R. Kaul, *Physical Review B* **88**, 220414 (2013).
 - ¹² A. Kitaev, *Ann. Phys.* **321**, 2 (2006).
 - ¹³ J. Chaloupka, G. Jackeli, and G. Khaliullin, *Phys. Rev. Lett.* **105**, 027204 (2010).
 - ¹⁴ H.-C. Jiang, Z.-C. Gu, X.-L. Qi, and S. Trebst, *Phys. Rev. B* **83**, 245104 (2011).
 - ¹⁵ J. Reuther, R. Thomale, and S. Trebst, *Phys. Rev. B* **84**, 100406 (2011).
 - ¹⁶ F. Trouselet, G. Khaliullin, and P. Horsch, *Phys. Rev. B* **84**, 054409 (2011).
 - ¹⁷ R. Schaffer, S. Bhattacharjee, and Y. B. Kim, *Phys. Rev. B* **86**, 224417 (2012).
 - ¹⁸ C. Price and N. B. Perkins, *Phys. Rev. Lett.* **109**, 187201 (2012).
 - ¹⁹ C. Price and N. B. Perkins, *Phys. Rev. B* **88**, 024410 (2013).
 - ²⁰ J. Chaloupka, G. Jackeli, and G. Khaliullin, *Phys. Rev. Lett.* **110**, 097204 (2013).
 - ²¹ S. Okamoto, *Phys. Rev. B* **87**, 064508 (2013).
 - ²² F. Trouselet, P. Horsch, A. M. Oleś, and W.-L. You, *Physical Review B* **90**, 024404 (2014).
 - ²³ I. Kimchi and Y.-Z. You, *Phys. Rev. B* **84**, 180407 (2011).
 - ²⁴ J. G. Rau, E. K.-H. Lee, and H.-Y. Kee, *Phys. Rev. Lett.* **112**, 077204 (2014).
 - ²⁵ V. M. Katukuri, S. Nishimoto, V. Yushankhai, A. Stoyanova, H. Kandpal, S. Choi, R. Coldea, I. Rousochatzakis, L. Hozoi, and J. van den Brink, *New Journal of Physics* **16**, 013056 (2014).
 - ²⁶ Y. Yamaji, Y. Nomura, M. Kurita, R. Arita, and M. Imada, (2014), [arXiv:1402.1030 \[cond-mat.str-el\]](https://arxiv.org/abs/1402.1030).
 - ²⁷ G. Khaliullin, *Prog. Theor. Phys. Suppl.* **160**, 155 (2005).
 - ²⁸ M. J. O'Malley, H. Verweij, and P. M. Woodward, *Journal of Solid State Chemistry* **181**, 1803 (2008).
 - ²⁹ J. C. Slater and G. F. Koster, *Phys. Rev.* **94**, 1498 (1954).
 - ³⁰ As in the case of hoppings the introduction of monoclinic distortion causes the $xy(z)$ bond to be inequivalent to the $yz(x)$ and $zx(y)$ bonds. This allows for an independent set of these exchanges on these bonds, and two different Γ' couplings.
 - ³¹ S. Sugano, *Multiplets of transition-metal ions in crystals* (Academic Press, 1970).
 - ³² We choose a basis for this doublet subspace so that magnetic moment operator is proportional to effective spin operators \vec{S}_i up to a diagonal g -factor matrix.
 - ³³ S. K. Choi, *APS March Meeting Talk, Denver* (2014).
 - ³⁴ I. Kimchi, R. Coldea, and A. Vishwanath, *ArXiv e-prints* (2014), [arXiv:1408.3640 \[cond-mat.str-el\]](https://arxiv.org/abs/1408.3640).
 - ³⁵ Y. Sizyuk, C. Price, P. Wölfle, and N. B. Perkins, *ArXiv e-prints* (2014), [arXiv:1408.3647 \[cond-mat.str-el\]](https://arxiv.org/abs/1408.3647).

Appendix A: Strong-coupling expansion

Since the atomic states of Ir are most easily presented using a quantization axis that goes perpendicular to the honeycomb

plane, it is natural to work in a pseudo-spin with these quantization axes. The pseudo-spin model is then given by

$$H = \sum_{(ij) \in \gamma} \left[J_1 S_i^z S_j^z + \frac{J_2}{2} (S_i^+ S_j^- + S_i^- S_j^+) + J_3 (S_i^+ S_j^+ e^{+i\phi_\gamma} + S_i^- S_j^- e^{-i\phi_\gamma}) + J_4 (S_i^z S_j^+ e^{-i\phi_\gamma} + S_i^+ S_j^z e^{-i\phi_\gamma}) + J_4 (S_i^z S_j^- e^{+i\phi_\gamma} + S_i^- S_j^z e^{+i\phi_\gamma}) \right], \quad (\text{A1})$$

where the exchanges J_1, J_2, J_3 and J_4 are related to J, K, Γ and Γ' through

$$J = \frac{1}{3} (J_1 + 2J_2 - 2J_3 + 2\sqrt{2}J_4), \quad (\text{A2a})$$

$$K = 2 (J_3 - \sqrt{2}J_4), \quad (\text{A2b})$$

$$\Gamma = \frac{1}{3} (J_1 - J_2 + 4J_3 + 2\sqrt{2}J_4), \quad (\text{A2c})$$

$$\Gamma' = \frac{1}{3} (J_1 - J_2 - 2J_3 - \sqrt{2}J_4). \quad (\text{A2d})$$

To work out the strong-coupling expansion we first rotate the kinetic parts in Eq. 9 into the [111] quantization axes and carry out the perturbation theory in this basis. Once complete, we use the relations above in Eq. A2a to find J, K, Γ and Γ' in the cubic axes. The full expressions for the exchanges discussed in Sec. II are given by

$$J = \frac{4}{27} \left[\frac{6t_1(t_1 + 2t_3) - 9t_4^2}{U - 3J_H} + \frac{9t_4^2 + 2(t_1 - t_3)^2}{U - J_H} + \frac{(2t_1 + t_3)^2}{U + 2J_H} + \sqrt{2} \left(\frac{3(t_2(4t_3 - 5t_4) + (7t_1 + t_3 - 4t_4)t_4)}{3J_H - U} + \frac{4t_2(4t_1 - t_3) + t_4(11t_1 + 13t_3) + 3t_4(4t_4 + 5t_2)}{J_H - U} - \frac{4(2t_1 + t_3)(t_2 + 2t_4)}{2J_H + U} \right) \theta \right], \quad (\text{A3a})$$

$$K = \frac{8J_H}{9} \left[\frac{(t_1 - t_3)^2 - 3(t_2^2 - t_4^2)}{(U - 3J_H)(U - J_H)} + \frac{\sqrt{2} (3(t_2 - t_4)t_4 + (t_3 - t_1)(2t_2 + t_4))}{(U - 3J_H)(U - J_H)} \theta \right], \quad (\text{A3b})$$

$$\Gamma = \frac{8J_H}{9} \left[\frac{3t_4^2 + 2t_2(t_1 - t_3)}{(U - 3J_H)(U - J_H)} - \frac{\sqrt{2} (t_2^2 + (t_1 - t_3)^2 + (t_1 - 3t_2 - t_3)t_4 + 5t_4^2)}{(U - 3J_H)(U - J_H)} \theta \right], \quad (\text{A3c})$$

$$\Gamma' = -\frac{8J_H}{9} \left[\frac{t_4(t_1 - t_3 - 3t_2)}{(U - 3J_H)(U - J_H)} - \frac{\sqrt{2} (2t_1(t_2 + t_3) - t_1^2 - (t_2 + t_3)^2 + (3t_2 + t_3 - t_1)t_4 - 4(t_2^2 + t_4^2))}{2(U - 3J_H)(U - J_H)} \theta \right], \quad (\text{A3d})$$

where we have expanded to leading order in trigonal distortion. To recover the results of Ref. 24 for the ideal octahedra, simply take $\Delta/\lambda \rightarrow 0$.